Physics of intrinsic rotation in flux-driven ITG turbulence

2012 Nucl. Fusion 52 063013

(http://iopscience.iop.org/0029-5515/52/6/063013)

Nucl. Fusion **52** (2012) 063013 (13pp) doi:10.1088/0029-5515/52/6/063013

Physics of intrinsic rotation in flux-driven ITG turbulence

S. Ku[1,2], J. Abiteboul[3], P.H. Diamond[2,4], G. Dif-Pradalier[3,4], J.M. Kwon[2], Y. Sarazin[3], T.S. Hahm[5], X. Garbet[3], C.S. Chang[1], G. Latu[3], E.S. Yoon[1,6], Ph. Ghendrih[3], S. Yi[2], A. Strugarek[3], W. Solomon[1] and V. Grandgirard[3]

[1] Princeton Plasma Physics Laboratory, Princeton, NJ, USA
[2] National Fusion Research Institute, Daejeon, Korea
[3] CEA, IRFM, F-13108 Saint-Paul-lez-Durance, France
[4] CMTFO and Department of Physics, University of California, San Diego, CA, USA
[5] Department of Nuclear Engineering, Seoul National University, Seoul, Korea
[6] Korea Advanced Institue of Science and Technology, Daejeon, Korea

E-mail: sku@pppl.gov

Received 27 September 2011, accepted for publication 22 February 2012
Published 27 April 2012
Online at stacks.iop.org/NF/52/063013

Abstract
Global, heat flux-driven ITG gyrokinetic simulations which manifest the formation of macroscopic, mean toroidal flow profiles with peak thermal Mach number 0.05, are reported. Both a particle-in-cell (XGC1p) and a semi-Lagrangian (Gysela) approach are utilized without *a priori* assumptions of scale separation between turbulence and mean fields. Flux-driven ITG simulations with different edge flow boundary conditions show in both approaches the development of net unidirectional intrinsic rotation in the co-current direction. Intrinsic torque is shown to scale approximately linearly with the inverse scale length of the ion temperature gradient. External momentum input is shown to effectively cancel the intrinsic rotation profile, thus confirming the existence of a local residual stress and intrinsic torque. Fluctuation intensity, intrinsic torque and mean flow are demonstrated to develop inwards from the boundary. The measured correlations between residual stress and two fluctuation spectrum symmetry breakers, namely $E \times B$ shear and intensity gradient, are similar. Avalanches of (positive) heat flux, which propagate either outwards or inwards, are correlated with avalanches of (negative) parallel momentum flux, so that outward transport of heat and inward transport of parallel momentum are correlated and mediated by avalanches. The probability distribution functions of the outward heat flux and the inward momentum flux show strong structural similarity.

(Some figures may appear in colour only in the online journal)

1. Introduction

Toroidal rotation of tokamak plasma is central to performance, since rotation stabilizes resistive wall modes and affect the L–H transition threshold, and may enhance confinement. In present day tokamaks, rotation is driven mainly by neutral beams, but beam drive is less effective in future devices, such as ITER. On the other hand, self-acceleration provides an intrinsic rotation—a spontaneous rotation without external momentum input [1]. Hence, understanding this phenomena is important for successful performance of future tokamak devices and tokamak reactors. Intrinsic rotation is produced by a component of the toroidal momentum flux not directly proportional to the toroidal velocity or its shear acting in concert with the boundary conditions. This non-Fickian flux is produced by a residual stress, driven by turbulence and ∇T_i, ∇P_i, ∇T_e, ∇n, etc.

The momentum flux driven by electrostatic turbulence is given by the Reynolds stress, so the radial component of Reynolds stress (i.e. radial flux) per unit mass per unit density of toroidal momentum can be decomposed as [2, 3]

$$\Pi_{r,\phi} = -\chi_\phi \frac{\partial \langle v_\phi \rangle}{\partial r} + V \langle v_\phi \rangle + \Pi^\mathrm{R}_{r,\phi},$$

where χ_ϕ is the turbulent momentum diffusion coefficient, V is the convective velocity, and $\Pi^\mathrm{R}_{r,\phi}$ is the residual stress per unit mass per unit density. In this paper, the stress per unit mass per density is called 'stress' for simplicity. Self-acceleration of a plasma from rest requires a non-zero residual stress $\Pi^\mathrm{R}_{r,\phi} \neq 0$ on the boundary. More generally, considerations of momentum balance dictate that

$$\left.\frac{\partial \langle v_\phi \rangle}{\partial r}\right|_\mathrm{bndry} = \left\{\left[\Pi^\mathrm{R}_{r,\phi} + V \langle v_\phi \rangle\right] / \chi_\phi\right\}_\mathrm{bndry},$$

i.e. the stationary toroidal intrinsic velocity gradient at the boundary is set by $\Pi^{\mathrm{R}}_{r,\phi}$ and $V\langle v_\phi\rangle$ at the boundary. For a no-slip boundary condition then, $\Pi^{\mathrm{R}}_{r,\phi}\big|_{\mathrm{bndry}}$ determines the rotation. This identifies the importance both of flow boundary conditions and of edge gradient effects on the rotation dynamics.

Note that the Reynolds stress equals the residual stress when the toroidal flow $\langle v_\phi\rangle$ and its gradient are zero. In order to explain the origins of intrinsic rotation, an intrinsic torque density—related to $\nabla\cdot\Pi_{r,\phi}$—has been proposed and linked to the asymmetry in the heat flux driven ambient turbulence. The most compelling experimental demonstration of the viability of the intrinsic torque concept are the cancellation experiments of Solomon *et al* [4] and Ida *et al* [5], in which momentum input opposite to the intrinsic rotation drastically reduces on-axis flow speeds and effectively cancels the intrinsic rotation profile. Indeed, a stationary plasma with nearly flat rotation profile results, in spite of applied torque! In this study, we perform related numerical simulations and so demonstrate the existence of a flux-driven residual stress. The results are used to elucidate the dynamics of residual stress and the intrinsic rotation.

A useful physical analogy which helps our understanding of intrinsic rotation is that of a heat engine [6, 7]. Loosely speaking, a heat engine converts some fraction of the free energy stored in a temperature differential or gradient to mechanical work. Similarly, there are many indications that the process of intrinsic rotation generation converts some fraction of the stored free energy implicit in a sustained temperature gradient ∇T to toroidal velocity. The temperature difference is converted to ordered kinetic energy of the flow. The microphysics of the residual stress is linked to turbulence spectral asymmetry. Of course, the local temperature gradient is in turn maintained by the local heat flux Q, so the latter emerges as the ultimate driver of the intrinsic rotation. In this regard, we note that while many simulations have addressed aspects of intrinsic rotation physics, none has as yet reported an unambiguously finite, unidirectional net toroidal rotation in flux-driven turbulence. In this paper, we explicitly demonstrate the viability of this scenario. Moreover, the heat engine analogy suggests that:

(i) the formation of intrinsic rotation profiles is closely related to the formation of temperature profiles, since $\nabla\langle T\rangle$ is seen as the fuel for the 'engine' which drives $\langle v_\phi(r)\rangle$. Thus, it is natural that intrinsic rotation drive is observed to be spatially correlated or co-located with regions of enhanced confinement, transport barriers, etc.

(ii) the *synergy* of thermal and flow or momentum boundary conditions is important to the development of this work. We demonstrate that the spatial proximity of an edge cooling layer (which supports a steepened ∇T, maintained by Q) and the no-slip boundary (which absorbs the stress transmitted to the boundary by the turbulent momentum flux) is crucial to the development of intrinsic rotation.

Nearly all previous simulation studies of intrinsic rotation physics focused entirely on the radial flux of toroidal momentum, and did not address actual rotation profile structure, the dynamics of intrinsic rotation build-up, and its evolution in the presence of heat flux-driven turbulence. Previous simulation study by Idomura using flux-driven gyrokinetic simulations presented global rotation profile, which shows dipole shape of rotation profile with co-current direction around magnetic axis and counter-current direction around edge with turbulence damping layers where flow is damping near boundaries [8].

Here, we present global, heat flux-driven gyrokinetic simulations which manifest the formation of macroscopic, unidirectional mean toroidal flow profiles which tend to be inwardly peaked with maximum thermal Mach number $M_{\mathrm{T}} = \langle v_\phi\rangle/v_{\mathrm{th}} \sim 0.05$ and which carry a net momentum (i.e. when radially integrated). The remainder of this paper is organized as follows. In section 2, the detailed simulation approach is described and toroidal momentum conservation of the gyrokinetic formalism is discussed. In section 3, the intrinsic rotation and the residual stress obtained from simulations are analysed. In section 4, the analysis of the spatio-temporal structure of the residual structure is presented. Section 5 presents discussion and conclusions.

2. Simulation approach and momentum conservation

In this study, the gyrokinetic turbulence codes XGC1p (a concentric circular magnetic geometry version of XGC1 [9]) and Gysela [10] have been used. Both codes solve the 5D gyrokinetic Vlasov equation derived from the electrostatic Lagrangian in gyro-centre variables [11, 12],

$$\begin{aligned}
&\frac{\partial f}{\partial t} + \dot{\boldsymbol{X}}\cdot\frac{\partial f}{\partial \boldsymbol{X}} + \dot{v}_\parallel\cdot\frac{\partial f}{\partial v_\parallel} = 0,\\
&\dot{\boldsymbol{X}} = (1/D)[v_\parallel\hat{b} + (mcv_\parallel^2/qB^2)\nabla\times\hat{b}\\
&\qquad + \{\boldsymbol{B}\times c(\mu\nabla B - q\boldsymbol{E})\}/qB^2], \qquad (1)\\
&\dot{v}_\parallel = -(1/mD)(\hat{b} + (mcv_\parallel/qB)\nabla\times\hat{b})\cdot(\mu\nabla B - q\boldsymbol{E}),\\
&D = 1 + (mcv_\parallel/qB)\,\hat{b}\cdot(\nabla\times\hat{b}).
\end{aligned}$$

Here f is the distribution function, $\boldsymbol{X}$ is the gyrocentre position in real space, $v_\parallel$ is the velocity of the gyrocentre parallel to the local magnetic field $\boldsymbol{B}$, $\hat{b} = \boldsymbol{B}/B$, $\mu = mv_\perp^2/2B$ is the magnetic moment, $\boldsymbol{E}$ is the gyro-averaged electric field, m is mass, and q is charge.

In the above conservative gyrokinetic formalism, the global gyrokinetic toroidal canonical angular momentum,

$$P_\phi^{\mathrm{G.C.}} \equiv \int\left(\frac{q}{c}\psi + mRv_{||}\frac{B_\phi}{B}\right) f\,J\,\mathrm{d}v_{||}\,\mathrm{d}\mu\,\mathrm{d}^3\boldsymbol{X} \qquad (2)$$

is conserved when the system is axisymmetric [13, 14], where superscript G.C. represents gyrocentre variable. Here ψ is the poloidal flux, B_ϕ is the toroidal component of magnetic field, R is the major radius of the gyrocentre and J is the Jacobian for the transformation from usual to gyrocentre phase space variables. However, the robustness of angular momentum conservation in gyrokinetic simulations has been questioned [15, 16]. Here, we demonstrate that simulation results obtained with XGC1p are not affected significantly by the error induced by non-conservation of angular momentum. The successful conservation of toroidal momentum in Gysela has already been exhaustively addressed in [14]. The angular momentum of the gyrocentres and the angular momentum of the particles

Table 1. Variations of toroidal angular momentum in Vlasov phase space and gyrokinetic phase space. Superscripts V and G.C. indicate Vlasov and gyrocentre variables respectively. $v_\perp$ represents perpendicular velocity including diamagnetic flow. Conservation of canonical angular momentum in the gyrokinetic formalism gives a small higher order toroidal momentum in real space due to profile changes. We assume the charge number of ion to be one for simplicity. $q = e$ for ion and $q = -e$ for electron.

	6D Vlasov space	5D gyrokinetic space
Conserved quantity (canonical angular momentum)	$P_\phi^{\mathrm{V}} \equiv \frac{q}{c} n^{\mathrm{V}} \psi + L_\phi^{\mathrm{V}}$, where $L_\phi^{\mathrm{V}} = \langle n^{\mathrm{V}} m R v_\phi \rangle$	$P_\phi^{\mathrm{G.C.}} \equiv \frac{q}{c} n^{\mathrm{G.C.}} \psi + L_\phi^{\mathrm{G.C.}}$, where $L_\phi^{\mathrm{G.C.}} = \langle n^{\mathrm{G.C.}} m R v_{\|} B_\phi / B \rangle$
Cancellation of $\frac{q}{c} n \psi$ of ions and electrons	Yes, by quasi-neutrality. $n_{\mathrm{i}}^{\mathrm{V}} = n_e$	No, by polarization density. $n_{\mathrm{i}}^{\mathrm{G.C.}} = n_e - \nabla \cdot (\rho_i^2 / 4\pi\lambda_D^2 e) E_r$
Conservation of toroidal angular momentum	$\Delta L_\phi = \Delta L_\phi^V = 0$	$\Delta L_\phi = \Delta L_\phi^{\mathrm{G.C.}} + \Delta \langle n m R v_\perp B_{\mathrm{p}} / B \rangle$ $= -\Delta \left(\frac{e}{c} n_p \psi \right) + \Delta \langle n m R v_\perp B_{\mathrm{p}} / B \rangle$

are different. Since the toroidal angular momentum of the particles is one of the conserved quantities, the time variation of the difference between the two momenta is an indication of errors in the momentum calculation in gyrokinetic simulation. These turn out to be negligible in the XGC1p simulations performed for this study, as shown below.

There can be two origins of the difference between the two toroidal momenta. One originates from the difference between gyrocentre of the gyrokinetic formalism and real particle position (the first term of equation (2)). The other is from the difference between $v_{||} R B_\phi / B$ and the actual toroidal velocity (i.e. the second term of equation (2)). Table 1 is a summary of those differences. In primitive Vlasov plasma and 5D gyrokinetic plasma, the canonical angular momenta, P_ϕ^{V} and $P_\phi^{\mathrm{G.C.}}$ are conserved, respectively, where superscript V represents 6D Vlasov plasma. In Vlasov plasma, the ion density is tightly bound to electron density by quasineutrality. Then, $\int (q/c) \psi f \mathrm{d}^3 v$ for ions and electrons cancel. Since the collisional exchange of momentum between electrons and ions is negligible, conservation of canonical angular momentum of ions implies conservation of angular momentum of ions. In contrast, the gyro-averaged gyrocentre density of ions, $n_{\mathrm{i}}^{\mathrm{G.C.}}$ can be different from electron density due to the polarization density, $n_{\mathrm{p}} = n_{\mathrm{i}}^{\mathrm{G.C}} - n_{\mathrm{e}}$ [17, 18]. In this case, $P_\phi^{\mathrm{G.C.}}$ is still conserved, as the change in kinetic angular momentum is compensated by the canonical momentum change from the polarization density, $e \Delta n_{\mathrm{p}} \psi / c$, where $n_{\mathrm{p}} \simeq \nabla \cdot (\rho_{\mathrm{i}}^2 / 4\pi\lambda_{\mathrm{D}}^2) E_r$ from gyrokinetic Poisson equation, ρ_{i} is the gyroradius and λ_{D} is the Debye length. Note that $\Delta n_{\mathrm{p}} = \Delta n_{\mathrm{i}}^{\mathrm{G.C.}}$ when electron density is constant. Here, we take the charge number of ion to be 1 for simplicity.

In addition to numerically induced non-conservation of $L_\phi^{\mathrm{G.C.}}$, which is evaluated from the second term of equation (2), the difference between the two angular momenta can produce a higher order toroidal flow. Since $L_\phi^{\mathrm{G.C.}}$ is only from parallel momentum, the toroidal component of perpendicular momentum should be considered to calculate the true toroidal momentum. Hence, the change in real toroidal momentum is the change in $L_\phi^{\mathrm{G.C.}}$ plus the change in the toroidal component of perpendicular momentum.

Note that all these aforementioned differences of angular momentum are higher order quantities in the conventional gyrokinetic formalism, and directly related to changes in the profiles. For example, consider a typical hydrogen plasma in a tokamak with $B_{\mathrm{T}} = 2\,\mathrm{T}$, $R_0 = 2\,\mathrm{m}$, $B_{\mathrm{p}}/B_{\mathrm{T}} = 0.1$, $R/L_T = 6$ and $T_{\mathrm{i}} = 2\,\mathrm{keV}$, where B_{T} and B_{p} are toroidal and poloidal magnetic field, R_0 is major radius, T_{i} is ion temperature and L_T is temperature gradient scale length. The higher order toroidal momentum from the polarization charge density can be estimated as follows. Considering sinusoidal shape of the radial variation of guiding centre density with wavenumber k and amplitude δn_{p}, the spurious canonical momentum is about $(e/c)\delta n_{\mathrm{p}} (\mathrm{d}\psi/\mathrm{d}r)(\pi/k)$. From the gyrokinetic Poisson equation, the amplitude (δn_{p}) and $E \times B$ speed (v_E) are related with $\delta n_{\mathrm{p}}/n_0 = (mc)/(eB) k v_E \sim k_\perp^2 \rho^2 e\phi/T$, where n_0 is unperturbed density. Hence, the spurious canonical momentum per particle becomes $\pi m R v_E B_{\mathrm{p}}/B$, after using $\mathrm{d}\psi/\mathrm{d}r = R B_{\mathrm{p}}$. The higher order flow is thus $\pi v_E B_{\mathrm{p}}/B$, approximately. Except in a steep gradient like the edge pedestal, $E \times B$ drift velocity is smaller than a few per cent of the thermal velocity. Using the above plasma parameters and assuming neoclassical radial E-field approximately $E = T/eL_T$, the $E \times B$ drift velocity is about 0.7% of thermal ion velocity. The $\pi B_{\mathrm{p}}/B$ factor reduces the higher order flow even further to 0.2% of thermal velocity. This estimation is based on v_E, assuming zero initial E-field. If the initial E-field is not zero, a factor of $\Delta v_E / v_E$ should be included and that would make the higher order flow become even smaller.

The higher order flow coming from neglecting of the toroidal component of the perpendicular flow can be decomposed into two major sources of perpendicular flows: $E \times B$ drift and diamagnetic flow. An estimation gives $R_0 B_{\mathrm{p}} \Delta (E_r - (\mathrm{d}P/\mathrm{d}r)/n)/B^2$ for the change in toroidal component of $E \times B$ flow and diamagnetic flow. Using the above tokamak parameters, the parallel component of diamagnetic flow due to temperature gradient is $300\,\mathrm{m\,s^{-1}}$, which is 6×10^{-4} of thermal ion (hydrogen) velocity. Since the variation of diamagnetic flow due to profile change is smaller, the spurious change in toroidal momentum from neglecting diamagnetic flow is insignificant when compared with the effects of momentum transport. From the neoclassical radial force balance equation, $E \times B$ drift from radial E-field is the same order of magnitude as diamagnetic flow, and the direction of $E \times B$ tends to cancel the diamagnetic flow. This makes the higher order flow from perpendicular flow even smaller than the estimated value, $6 \times 10^{-4} v_{\mathrm{th}}$.

Considering conventional tokamak parameters for core plasmas, the higher order flow generation is much smaller than the turbulence momentum transport. However, during the edge pedestal formation, the change in $E \times B$ drift velocity becomes a fraction of thermal velocity, and a possible higher order flow needs to be considered with care. For simulations exhibiting sharp and large profile changes, corrections to the angular momentum are required to calculate the toroidal momentum accurately. A numerical method that conserves the real toroidal momentum using multi-scale correction will be presented in

Table 2. Table comparing the imposed boundary condition and consequence for the thermal and momentum channel.

Channel	Boundary condition (outer)	How enforced	Consequence
Ion temperature	Edge cooling applied $r > 0.78a$	Particle velocity is rescaled with momentum conservation to reduce the temperature according to a give cooling power.	Formation of steepened $\nabla T_i/T_i$ for $r > 0.7a$
Toroidal velocity	No slip (i.e. $v_\phi = 0$) applied $r > 0.87a$	Strong friction with exponential decay of momentum. Decay constant is $40/\Omega_i$	$\langle v_\phi \rangle \to 0$ at the boundary layer. Net toroidal spin-up driven by ∇T via transmission of stress to boundary by turbulent transport.

the near future. In the XGC1p simulations presented in this paper, we always considered a near steady-state plasma, so that the momentum difference due to the change in gyrocentre density and temperature are less than 0.02% of ion thermal velocity. These are negligible as compared with the peak intrinsic parallel flow generated in the simulations.

Unlike conventional delta-f gyrokinetic codes, which calculate only turbulence perturbation with assumed scale separation between turbulence and mean profiles (ignoring ∇B-drift in the weight evolution equation from equation (1)), both XGC1p and GYSELA evolve the turbulence and mean fields self-consistently by keeping all of the time evolution of f.

The numerical approach of XGC1p is the particle-in-cell method. A no-slip boundary condition is used to constrain the flow at the outer boundary assuming that the rotation of edge is small due to edge effects. XGC1p enforces a no-slip boundary condition by applying a very high friction to the parallel flow near the outer boundary. To implement the high friction force, XGC1p calculates flux-averaged parallel flow of small layers near outer boundary and periodically shifts the particle distribution towards zero flow. The period is about $100/\Omega_i$, where Ω_i is gyrofrequency of ion. The period is much smaller than the momentum transport time scale and much larger than simulation time step, which enables efficient simulation. Table 2 shows the boundary condition of XGC1p.

GYSELA uses the semi-Lagrangian numerical scheme and solves the full distribution function, implying no scale separation between equilibrium and perturbations. As in the case of XGC1p, a no-slip boundary condition is imposed at the outer boundary. At the inner boundary, a vanishing gradient is imposed and the toroidal flow is not constrained. An *ad hoc* diffusion, non-vanishing in small regions near the radial boundaries of the domain, is included in the gyrokinetic equation. This term provides an efficient coupling to the thermal bath and no-slip condition at the edge.

It is important to note that this implementation of the no-slip boundary condition does *not* damp the turbulent fluctuations near the boundary and so allows the transmission of stress into the boundary layer by turbulent transport. This interaction between the plasma and the boundary through turbulence is crucial to achieving global spontaneous spin-up of tokamak plasma without external torque input. From a more general point of view, it is obvious that any conserved quantity such as the toroidal momentum can reach non-vanishing volume averaged values if and only if the system is open, i.e. if it exchanges information with the exterior via the boundary conditions. Hence, if transmission of stress to the boundary (by turbulence in XGC1p) is inhibited, net radially

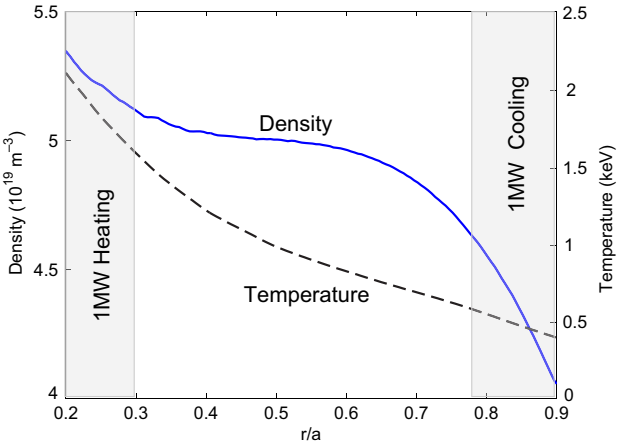

Figure 1. Density and temperature profile used in XGC1p. The temperature profile is when near steady state is obtained. Locations where heating and cooling are applied are shown.

integrated rotation is impossible. In that case, oppositely directed toroidal counter flows, with no *net* momentum, will result. This observation underscores the sensitivity of intrinsic rotation to the boundary conditions on *all* of flow, heat and fluctuations. Note that, in GYSELA, the dissipative buffer regions ensure exchange of information, including momentum, with the exterior. In this case, such an exchange is mostly controlled by the *ad hoc* dissipation, with a minor contribution from fluctuations which tend to be damped in these boundary regions.

In this study, the turbulence is flux-driven, and the dynamics responds to heat sources and sinks in the plasma. The regions where the source(sink) are applied are localized near the inner(outer) boundary, so as not to interfere with the turbulence in the middle (figure 1). In XGC1p, the heating (source) and cooling (sink) conserve momentum. The perpendicular velocity ($v_\perp$) and parallel velocity ($v_{||}$) of each particle are multiplied by a factor of α and parallel velocity is adjusted by β periodically, ($v_\perp^{\rm new} = \alpha v_\perp^{\rm old}$, $v_{||}^{\rm new} = \alpha v_{||}^{\rm old} + \beta$). α and β are determined to conserve energy and momentum, considering the external heating power and the external torque. The upshot of the edge cooling is to allow the formation of a steep edge temperature gradient close to the plasma boundary. In GYSELA also, the heating occurs near the inner boundary. The heat sink however is differently modelled: no cooling is applied and the diffusive term near the outer boundary acts as the energy sink. The source term in GYSELA is a versatile source which can allow for separate injections of heat, momentum and vorticity [19]. As a result of this constraint, this source

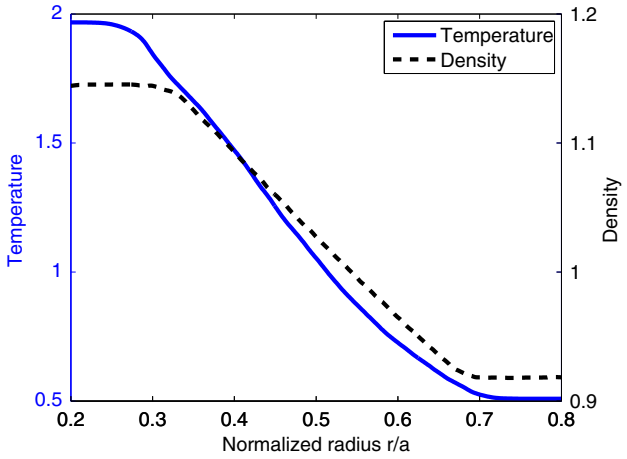

Figure 2. Density and temperature profile used in GYSELA. The temperature and density are nomalized. $\rho_* = 1/512$ and $\nu_* = 0.1$.

term can be chosen to be either isotropic or anisotropic in velocity space. For the simulations presented here, only a momentum-conserving heat injection is included. Details of other parameters are given in [19].

The safety factor $q(r)$, the density, and the temperature profiles used in XGC1p are adopted from the DIII-D experiments (H-mode plasma with NBI heating) described in [4]. Since the temperature profile in full-f simulation is evolving self-consistently, the detailed structure of the temperature profile when we set zero initial flow is different from the experimental data. The temperature profile is from a (near) steady state with 1 MW heating and cooling. The density and temperature profile of XGC1p are shown in figure 1. The density and temperature profile used in GYSELA are typical L-mode like plasmas. The profiles are shown in figure 2. The ρ_* is 1/298 for XGC1 and 1/512 for GYSELA, where ρ_i is the characteristic ion gyroradius and ρ_* is ρ_i over minor radius. The grid sizes (radial, poloidal, toroidal) of XGC1p simulation are (150, 300, 64) and those of GYSELA are (1024, 1024, 128). The poloidal grid size of XGC1p is an averaged value, since the poloidal grid number is varying in radius. In both codes, only the ion distribution functions are calculated and electrons are assumed to respond adiabatically to the electric potential on a flux surface. Coulomb collisions are not included in the XGC1p simulations to study the effect of pure turbulence, while a Fokker–Planck operator acting on $v_\parallel$ is included in GYSELA [20]. The collisionality $\nu_* = 0.1$ and the total simulation time is roughly 0.3 collision time for GYSELA simulation. Therefore collisional effects are not expected to dominate the processes considered in the article.

Both codes compute the time evolution of the temperature profile given the source (sink) profiles. The stationary state can be obtained with long simulations for a much larger time scale than the transport time scale. However, due to limitations on available computational resources, we stop the simulations near a stationary state for temperature and turbulence intensity. We emphasize, however, that in this state, the rotation profile is not yet stationary and the intrinsic flow is still developing.

The temperature profile still varies up to a few per cent during the simulation in the radial region $0.3 < r/a < 0.8$. The simulation results from XGC1p in the cancellation

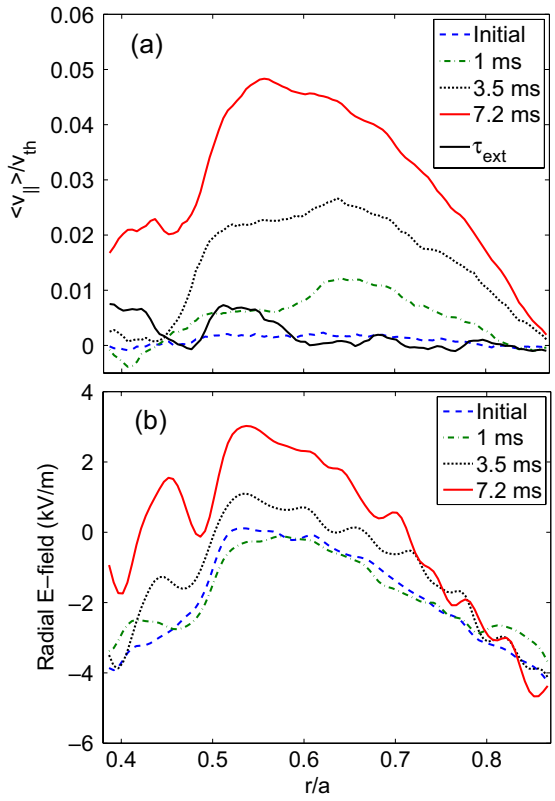

Figure 3. (*a*) Parallel flow develops in XGC1p without torque at $t = 0$, 1, 3.5 and 7.2 ms. (0, 170, 580 and 1200 R_0/v_{th}) Black solid line shows parallel flow with external torque. $M_T \simeq 0.05$ is achieved at 7 ms, and the external torque suppresses it to $M_T < 0.01$ globally. (*b*) Radial electric field profile at the corresponding time.

experiment figures 3 and 5 are obtained using the following procedure. (i) Achieve a near steady temperature profile for a given heating and cooling profile. (ii) Suppress the parallel flow so that the plasma is nearly at rest. (iii) Restart the simulation ($t = 0$ at graphs) with negligible initial flow and observe turbulence induced momentum transport with/without external torque. The results shown in this work are from stage (iii) of the procedure. A similar cancellation experiment in GYSELA is not shown here and a more classical setup is shown: the turbulence is initialized in the central region $0.35 < r/a < 0.65$ of the box, spreads throughout the box and adjusts to the source (sink) conditions. Whilst doing so an initially vanishing parallel flow builds up where the turbulence is initially strong and spreads radially.

In the simulations presented here, parallel flow and toroidal flow are very close to each other, so the terms are interchanged without distinction. The XGC1p simulation has been performed on the Cray-XT5 machine of National Centre for Computational Sciences and Cray-XE6 machine of National Energy Research Scientific Computing Centre. The GYSELA computations were performed at the Centre de Calcul Recherche et Technologie.

3. Intrinsic rotation and intrinsic torque

Figures 3(*a*) and 4 show the evolution of intrinsic rotation in ITG simulations using respectively XGC1p and GYSELA

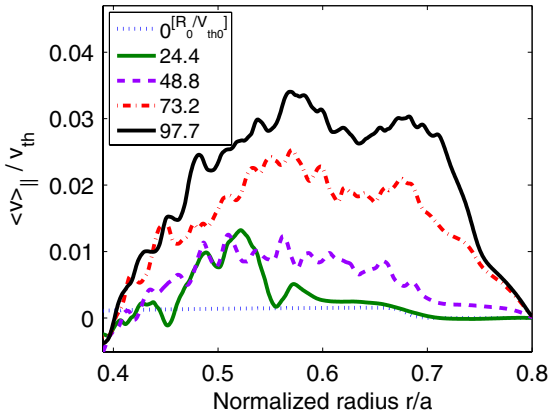

Figure 4. Parallel flow develops in GYSELA without torque at $t = 0$, 24.4, 48.8, 73.2 and 97.7 $R_0/v_{\rm th}$. 110 $R_0/v_{\rm th}$ is corresponding to 1 ms.

without an external torque. For XGC1p, the magnetic geometry is approximated by a concentric circular torus with 1.93 T magnetic field on axis, 1.7 m major radius, and 0.6 m minor radius. ρ_* is about 1/298. 1 MW heating (cooling) is applied near the magnetic axis (the last closed flux surface) to the ion species in the regions of $0.17 < r/a < 0.3$ ($0.78 < r/a < 0.92$), respectively. An external torque is then applied to cancel the rotation in the region of $0.4 < r/a < 0.8$. The simulation started from zero initial flow and a near steady-state temperature profile. The electrostatic potential Φ_{out} at the outer boundary is held fixed (to zero in the case shown). A mean parallel flow is generated and achieves a peak Mach number $M_{\rm T} \simeq 0.05$, in the co-current direction after 7 ms ($\simeq 1200 R_0/v_{\rm th}$, red solid line). A saturated parallel flow is not achieved during 7 ms and the peak of the rotation curve is still increasing and propagating inward toward the core. Since diffusion term is growing as the global parallel flow is being generated, the speed of increment of the peak velocity becomes smaller at the end of simulation. This state of continuing inward flow profile development explains the hollowing of the rotation profile evident in figure 3. Figure 3(*b*) shows evolution of radial electric field when the flow is building up.

In figure 4, a similar result is obtained using the GYSELA code, for a simulation at $\rho_* = 1/512$. The same simplified magnetic geometry was used, while the temperature and density profiles were initialized with constant R/L_T and R/L_n throughout most of the simulation domain $0.35 < r/a < 0.65$, with $R/L_T = 11.5$ and $R/L_n = 2$ at $r/a = 0.5$. The simulation started from nearly zero initial flow. A peak Mach number of $M_{\rm T} \simeq 0.035$ in the co-current direction is found and is still developing.

The existence of an intrinsic torque density due to turbulent residual stress is established using simulations in toroidal geometry, with a no-slip boundary condition. The black solid line of figure 3 shows the outcome of the numerical experiment which corresponds to Solomon's physical experiment using external torque to off-set or cancel intrinsic torque. The whole simulation with external torque consists of a series of short simulations. At the end of each short simulation, the magnitude of the torque input and its radial profile were slightly adjusted to avoid excessive or

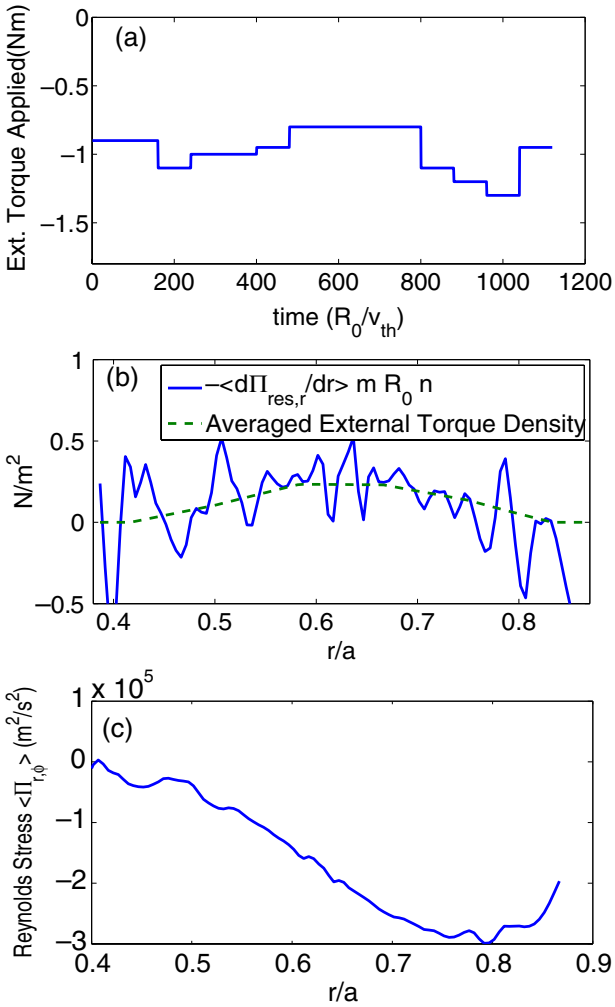

Figure 5. (*a*) Time variation of total external torque in XGC1p. (*b*) Time-averaged intrinsic torque (solid line) and external torque profile (dotted line). The sign is inverted for clear comparison. (*c*) Time averaged Reynolds stress. Since parallel flow is near zero globally, this is primarily residual stress.

insufficient momentum input. About 1 Nm of counter direction torque is applied during the simulation, and the external torque input tracks the self-generated torque from the Reynolds stress (figures 5(*a*) and (*b*)). A local value of the toroidal Mach number $M_{\rm T} <\simeq 0.01$ is maintained during the simulation. Note that *global* cancellation of the rotation was achieved. These results constitute a clear demonstration-of-principle of the concept of a local, intrinsic torque density and its relation to intrinsic rotation. Hence, the Reynolds stress (see figure 5(*c*)) can be interpreted as consisting of a residual stress as well as a turbulent viscous flux. Both contributions are flux driven.

It is this residual stress which drives the co-current intrinsic torque. Indeed, it is possible to estimate both the injection rate of the parallel velocity from figures 1 and 3, and the divergence of the (r, ϕ) component of the residual stress tensor from figure 5(*c*). On the one hand, one finds at $\rho = 0.6$ an increase in $v_\parallel$ of the order of $\Delta v_\parallel / v_{\rm th} \approx 0.0442$, with $v_{\rm th} \approx 2.8 \times 10^5$ m s^{-1}, in $\Delta t = 7.2 \times 10^{-3}$ s. This leads to $\Delta v_\parallel / \Delta t \approx 17 \times 10^5$ m s^{-2} (figures 1–3). On the other hand, the corresponding divergence of the residual stress is of the

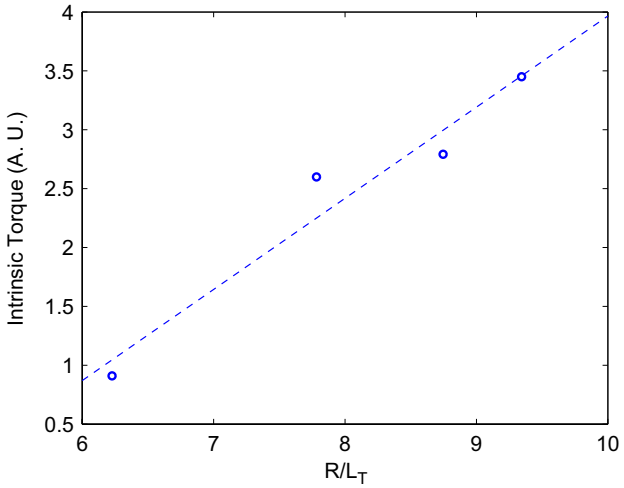

Figure 6. Scaling of intrinsic torque with respect to normalized ion temperature gradient scale length R/L_T ($L_T \equiv T/\nabla T$) in XGC1p. The x-axis is R_0/L_T, where R_0 is major radius of magnetic axis. The dashed line is from linear regression.

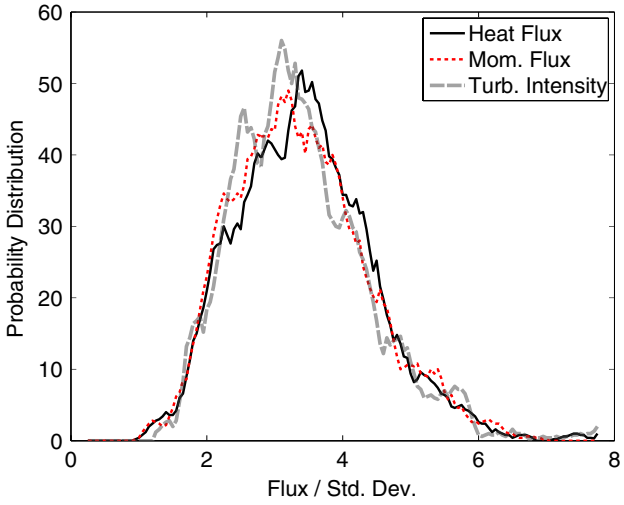

Figure 7. Probability distribution function of outward heat flux (solid), the negative of the momentum flux (dotted), and turbulenc intensity (dashed) at $r/a = 0.76$ in XGC1p simulation with $R/L_T \simeq 6$. The x-axis is normalized in the standard deviation. The two distribution functions are similar, including mean value. Note that, for cancellation simulations, the non-zero mean momentum flux, which gives co-current rotation, is cancelled by external torque so as to keep the plasma stationary.

order of $\nabla_r \Pi_{r\phi} \approx \Delta\Pi_{r\phi}/\Delta r \approx -3.8 \times 10^5/(0.34 \times a) \approx -18.6 \times 10^5\,\mathrm{m\,s^{-2}}$ (figure 5(*c*)). It appears that $\Delta v_\parallel/\Delta t + \Delta\Pi_{r\phi}/\Delta r \sim 0$. This rough numerical estimate confirms that, in this case, the residual stress is the main contributor to the time evolution of the parallel velocity.

A key question concerns the scaling of the intrinsic torque with temperature gradients or $R/L_T - R/L_{T_{\mathrm{crit}}}$, equivalently. Obviously, since heat flux drives the turbulence and the turbulence drives the intrinsic torque, the latter (intrinsic torque) should increase with $\nabla T/T$. However, the form (i.e. exponent) of the R/L_T dependence is of interest in the context of comparison with both experimental results and theoretical predictions. Figure 6 shows the scaling of intrinsic torque with respect to temperature gradient scale length (L_T). Various sets of heating/cooling powers are applied and temperature profiles adjust self-consistently. The intrinsic torque and effective L_T are obtained by averaging these values over the mid-minor radius region $0.4 < r/a < 0.6$. The dashed line is obtained from a linear regression. The scaling result shows an approximate linear proportionality of intrinsic torque to R/L_T. This relation is consistent with recent experimental findings and with theoretical predictions. Experimental results in ITB [5] and H-mode and I-mode [21] all suggest a rough proportionality of intrinsic rotation, and thus (indirectly) intrinsic torque, to R/L_T. These results are consistent with those of the simulation, though the reader should take care to note that the plasma confinement regime studied here is neither an ITB nor an ETB. Theoretical calculations [7] also suggest intrinsic torque, $\tau_{\mathrm{intr}} \propto R/L_T$ though again these apply to regimes with a dominant symmetry breaking by $E \times B$ shear (i.e. as for a transport barrier), which does not occur in the cases studied here. Nevertheless, these results, which are the first of their kind for stationary flux-driven ITG turbulence with no-slip boundary conditions on $v_{||}$, *do* suggest a nearly direct proportionality of τ_{intr} with R/L_T, and so are consistent with the fundamental underpinnings of the paradigm of intrinsic rotation as heat engine.

In the simulations, the turbulence arises where most unstable: near the outside boundary in XGC1p and in the central region in GYSELA. The turbulence propagates inward in XGC1p and both inwards and outwards in GYSELA as intensity pulses and these pulses drives an outward heat flux and inward momentum flux in XGC1p (outward heat flux and both inward and outward momentum flux in GYSELA). The inward momentum flux is responsible for the build up of intrinsic rotation. Figure 7 shows the probability distribution (PDF) in XGC1p of outward heat flux $Q = \langle \tilde{v}_r \tilde{T} \rangle$, the *negative* of the momentum flux $\langle \tilde{v}_r \tilde{v}_\phi \rangle$, and the turbulence intensity $e^2\Phi^2/T^2$ at $r/a = 0.76$. The overlay, of course, indicates that the momentum flux is inward. To compare the PDFs, the x-axis is normalized by the standard deviation of each PDF. The three PDFs of XGC1p are very similar to one another, including the normalized mean value. The same similarity is observed at the radial position where significant intrinsic torque exists. This tells us that avalanches, which transport heat outwards, can drive parallel momentum inwards with increased turbulence, and is further evidence for non-diffusive, temperature gradient driven nature of the momentum flux due to residual stress. In the regions where the intrinsic torque is small and the turbulence is reduced due to strong $\boldsymbol{E} \times \boldsymbol{B}$ shear, the PDF of negative momentum flux (inward propagation of momentum) deviates from the PDF of positive heat flux (outward propagation of heat). In the regions, the mean momentum flux is reduced, as compared with the regions with strong heat avalanches.

Figure 8 shows the PDFs for heat transport, momentum transport, and turbulence intensity obtained from the GYSELA simulation presented above. For each flux, because the time average varies slightly at different radial positions, the PDF is actually for $\Gamma - \langle\Gamma\rangle$ where $\langle\Gamma\rangle$ is the time-averaged flux at a given radial position. The PDFs obtained from the GYSELA simulation are notably different from the XGC1p results in figure 7, in particular the overlaying of the PDFs of heat and momentum transport is not recovered. One possible reason

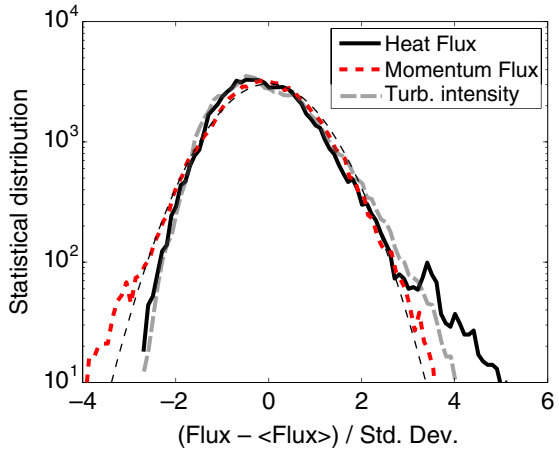

Figure 8. Probability distribution function of heat flux (solid), momentum flux (dotted), and turbulence intensity (dashed) around mid-radius $r/a = 0.5$ in GYSELA simulation with finite rotation. A Gaussian fit is also plotted for comparison.

may reside in the different profiles used by the simulation. In the XGC1p simulation, a steep temperature gradient is maintained near the outer boundary, thus turbulence is most active in the outer region of the plasma and the momentum flux is always inward, generated at the edge and flowing in the direction of the core. On the other hand, the profiles used in the GYSELA simulation lead to an active turbulence throughout the simulation domain. Thus, in terms of momentum flux, both inward and outward propagation are observed, while the flux-averaged heat flux is always outward. Despite these differences, the transport of both heat and momentum are found to exhibit large-scale events, as evidenced by the large tails in the PDFs in figure 8. This can be quantified by computing the excess kurtosis of the distributions, defined as $Ku(f) = \langle (f - \bar{f})^4 \rangle / \langle (f - \bar{f})^2 \rangle^2 - 3$ where $\bar{f}$ is the mean of f, which is vanishing for Gaussian statistics and positive for flat distributions, indicating heavy tails. Excess kurtoses of approximately 1.67 and 0.52 are obtained for respectively the heat and momentum flux PDFs, confirming the intermittent nature of the observed turbulent transport. The PDF of the turbulence intensity is rather similar to the PDF of the heat flux.

Finally, we comment here that in these simulations, while the turbulence is stationary, the rotation profile is still evolving and so the intrinsic rotation is still increasing while the profile builds inwards from the edge toward the centre. As noted above, this explains the hollowing of the rotation profile shown in figure 3. Thus $\partial_t \int dr \langle v_\phi(r) \rangle \neq 0$, and the net intrinsic torque (drive) is still in the process of overcoming the net viscous torque. In a stationary state, we anticipate rough equality between turbulent viscous and diffusive stresses, so $-\chi_\phi \partial \langle v_\phi \rangle / \partial r + \Pi^{\rm intr}_{r,\phi} \approx 0$, indicative of a balance between the co-existing tendencies of the turbulence to both accelerate and decelerate the plasma. Thus we speculate that in a steady heat flux driven state close to that shown here in GYSELA, the heat flux PDF will remain similar in structure to that shown in figures 7 and 8, while the magnitude of the centroid of the momentum flux PDF should decrease toward zero—i.e. the steady-state momentum flux PDF should approach symmetry about $\Pi = 0$, as hinted at in figure 8. These speculations

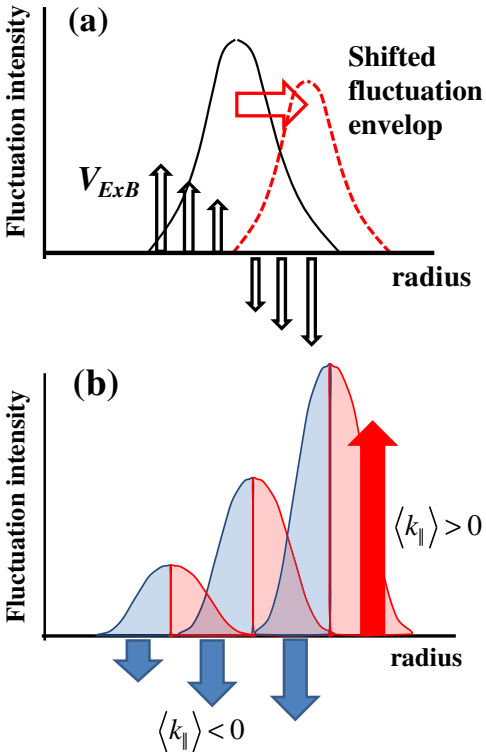

Figure 9. Cartoon to show $\langle k_{||} \rangle$ symmetry breaking caused by (*a*) $E \times B$ flow shear induced fluctuation envelop shift and (*b*) the radial inhomogeneity of fluctuation intensities.

will be tested in future studies, which will demand extensive computational resources.

We speculate here that the somewhat counter-intuitive claims that core MHD activity appears to enhance intrinsic rotation [22] may be due to the fact that avalanches carry simultaneously heat outwards and parallel momentum inwards, as described above. In particular, the sawtooth crash triggers an outward heat pulse, which in turn could result in inward parallel momentum propagation, leading to an increase in (intrinsic) rotation.

As part of this study, we also compared two theoretical candidate mechanisms for the symmetry breaking required for the residual stress, namely k-parallel symmetry breaking by $E \times B$ shear and by intensity gradient [23–25]. These two mechanisms are related but complementary, in that $E \times B$ symmetry breaking creates a net $\langle k_{||} \rangle$ by shifting the centroid of the spectral distribution while intensity gradients create a net $\langle k_{||} \rangle$ by weighting various pieces of the spectral profile differently, according to the net intensity profile gradient (see figure 9). Note that the two are likely to occur in synergy—a region of enhanced $E \times B$ shear will likely be banded by small zones of large profile *curvature*, which are related to intensity gradients. Furthermore, in the cases studied here, which are *not* transport barriers dominated by strong shear, we can expect both effects to contribute to symmetry breaking. In the following analysis of residual stress correlation with $\langle V_E \rangle'$ and fluctuation intensity gradients, we shall indeed see that *both* are correlated (roughly comparably) with the residual stress and intrinsic torque.

Figures 10 and 11 show the correlations from respectively XGC1p and GYSELA between residual stress,

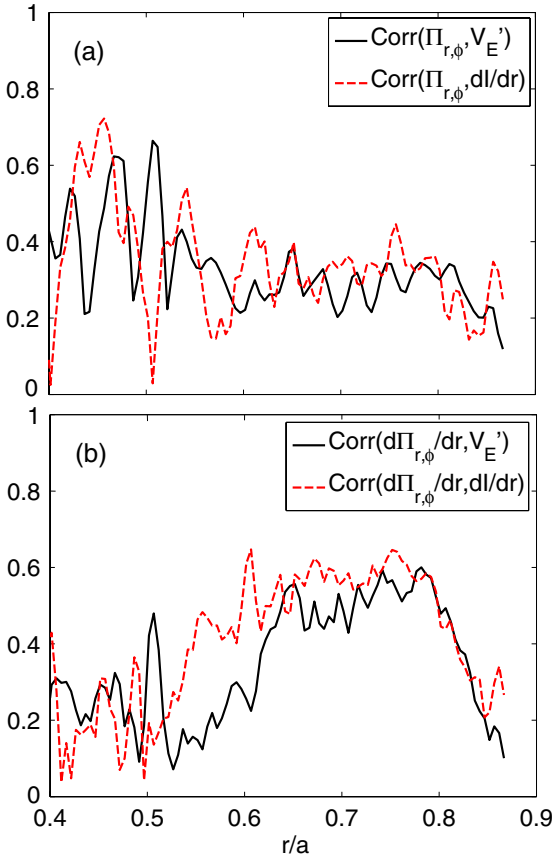

Figure 10. Correlation results from XGC1p with $R/L_T \simeq 6$. (a) Correlation between the residual stress and the symmetry breakers. (b) Correlation between intrinsic torque and the symmetry breakers. Solid line represents $E \times B$ shear and dashed line represents intensity gradient.

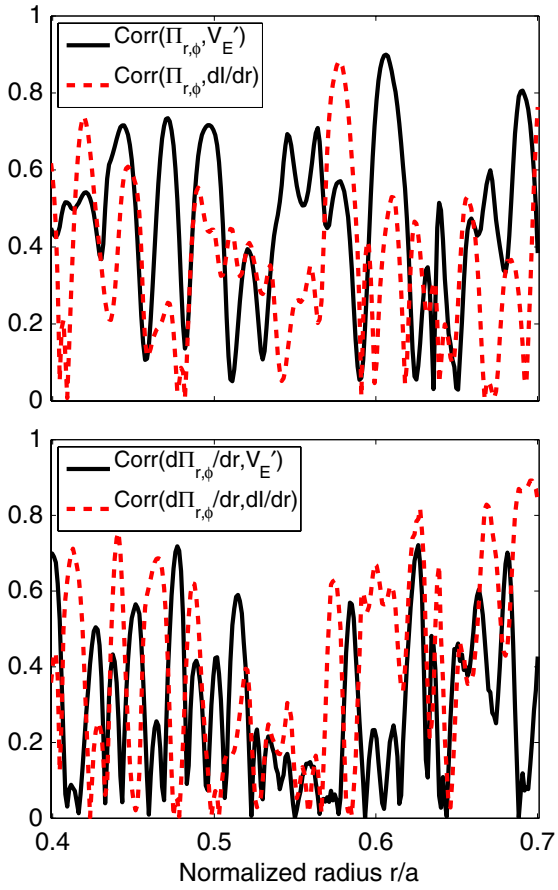

Figure 11. Correlation results from GYSELA. (a) Correlation between the residual stress and the symmetry breakers. (b) Correlation between intrinsic torque and the symmetry breakers. Solid line represents $E \times B$ shear and dashed line represents intensity gradient.

divergence of residual stress (intrinsic torque), $E \times B$ shear, and divergence of intensity gradient. The correlations are obtained in Fourier space, with $C(a,b) = \sum_{\omega>0} A_\omega B_\omega^* / \sqrt{\sum_{\omega>0} A_\omega A_\omega^* \sum_{\omega>0} B_\omega B_\omega^*}$, where A_ω and B_ω are Fourier transform of a and b in time domain, (*) represents complex conjugate. The magnitudes of correlations are shown in the figure. For example, anti-correlation gives 1 instead of -1. Due to the strong correlation between residual stress and turbulence intensity, intrinsic torque and intensity gradient (which are radial derivatives of residual stress and turbulence intensity) show strong correlation with one another. $E \times B$ shear also shows a strong correlation with intrinsic torque in XGC1p: ~0.6 whilst it is smaller in GYSELA: ~0.3. On the other hand, one finds a strong correlation of $E \times B$ shear with residual stress in GYSELA (~0.6) and a slightly smaller one (~0.4) in XGC1p. The different level correlations between XGC1p and GYSELA possibly come from the existence of external torque in addition to the different ρ_*, plasma profile, and boundary condition. Interestingly, intensity gradient shows similar levels of correlation as does $E \times B$ shear, and is even larger in some regions. This shows the possible importance of intensity gradient as a major k-parallel symmetry breaking mechanism.

Figure 12 shows the phase lag between those quantities in XGC1p. Intensity gradient and $E \times B$ shear show an approximately $\pi/2$ and $-\pi/2$ phase lag relative to residual stress, where $r/a > 0.6$. The phase lag between $E \times B$ shear and intensity gradient is about $\pi/2$, too. The phase lag between residual stress and symmetry breakers is consistent with the picture of a drift-acoustic response of parallel velocity

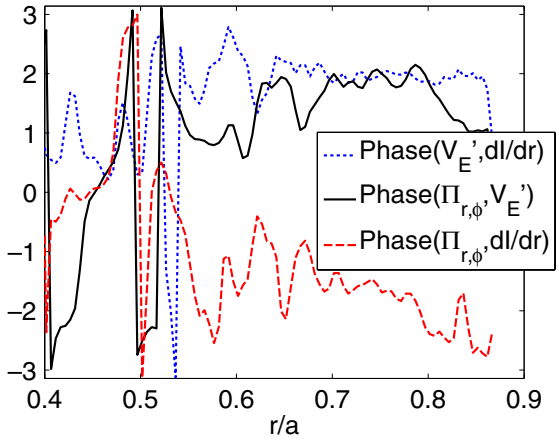

Figure 12. Phase of (a) the correlation between residual stress and symmetry breakers; phase of (b) correlation between intrinsic torque and symmetry breakers in XGC1p with $R/L_T \simeq 6$. Solid line represents $E \times B$ shear and dashed line represents intensity gradient.

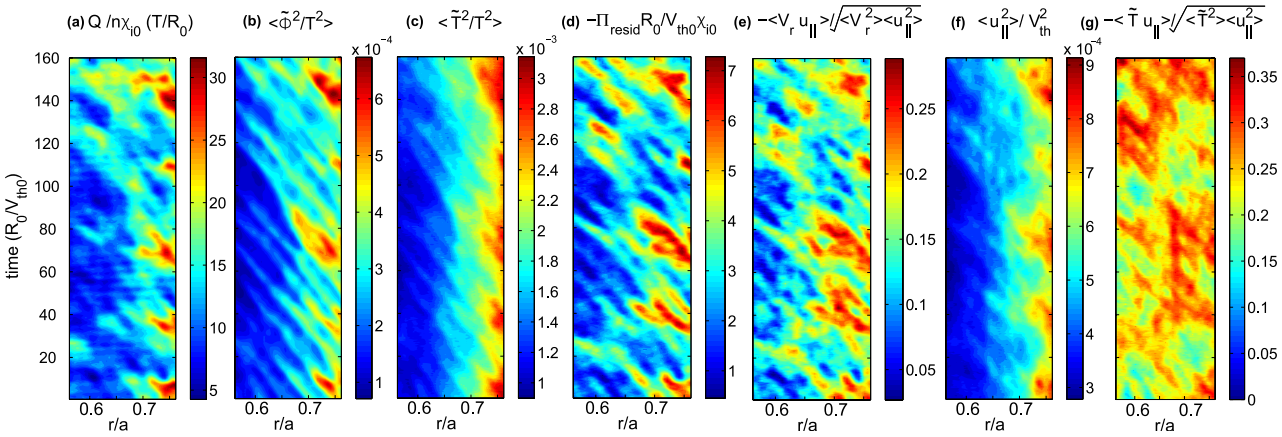

Figure 13. Space–time graphs in XGC1p ($R/L_T \simeq 8$) of (a) normalized heat flux Q_i, (b) turbulence intensity $\langle(e\tilde{\phi}/T)^2\rangle$, ($c$) perturbed temperature intensity $\langle(\tilde{T}/T)^2\rangle$, ($d$) the residual stress $\langle\tilde{v}_r\tilde{v}_{||}\rangle_{\text{non-diff}}$, ($e$) the cross-phase between $\tilde{v}_r$ and $\tilde{v}_{||}$, (f) the intensity of parallel flow fluctuations $\langle\tilde{v}_{||}^2\rangle$ omitting $m = 0$ and $m = 1$ contributions, (g) the cross-phase between $-\tilde{T}$ and $\tilde{v}_{||}$. The x-axis is normalized minor radius, and the y-axis is normalized time. T_0(1 keV), χ_{i0}(1 m^2 s^{-1}), R_0(1.7 m) and $v_{\text{th}0}$(3.1×10^5 m s^{-1}) are constants. T and v_{th} are functions of minor radius.

to pressure as the mechanism which relates the Reynolds stress to the ultimate ∇T, ∇P drive. In particular, the phase lag between parallel gradient of pressure and parallel velocity is convolved with spectrally averaged k-parallel to form the residual stress, suggesting that the stress is formed by the acoustically driven fluctuating parallel velocity $\tilde{v}_{||}$. The additional phase lag is thus likely a consequence of drift-acoustic dynamics. In the event that significant mean flow shear $\partial\langle v_{||}\rangle/\partial r$ has built up, we can expect $\tilde{v}_{||} = -\tau_c\tilde{v}_r\partial\langle v_{||}\rangle/\partial r - \tau_c\nabla_{||}\tilde{P}/n$, so $\tilde{v}_{||}$ should exhibit a phase lagged dependence on *both* $\tilde{v}_r\partial\langle v_{||}\rangle/\partial r$ as well as $\nabla_{||}\tilde{P}$, so correlation with $\nabla_{||}\tilde{P}$ should be lower in the case of a stationary flow profile. Further studies with stationary profiles will address this point.

4. Space–time development of residual stress and turbulence intensity profile

It is instructive to compare the space–time evolution of various quantities which are relevant to the build-up dynamics of the intrinsic velocity profile. These quantities are:

(a) the normalized fluctuation-driven heat flux Q_i
(b) the turbulence intensity field $\langle(e\tilde{\phi}/T)^2\rangle$
(c) the perturbed temperature intensity $\langle(\tilde{T}/T)^2\rangle$
(d) the residual stress $\langle\tilde{v}_r\tilde{v}_{||}\rangle_{\text{non-diff}}$
(e) the cross-phase between $\tilde{v}_r$ and $\tilde{v}_{||}$ in $\langle\tilde{v}_r\tilde{v}_{||}\rangle$, i.e. $\phi = \langle\tilde{v}_r\tilde{v}_{||}\rangle/\langle\tilde{v}_r^2\rangle\langle\tilde{v}_{||}^2\rangle$
(f) the intensity of parallel flow fluctuations $\langle\tilde{v}_{||}^2\rangle$, omitting $m = 0$ and $m = 1$ contributions (due to GAMs)
(g) cross-phase between $-\tilde{T}$ and $\tilde{v}_{||}$

These are shown for XGC1p in figure 13 and for GYSELA in figure 14. In figure 14, the residual stress for non-stationary profiles with increasing rotation is effectively the fluctuation Reynolds stress. Time (y-coordinate) is normalized to R_0/v_{ti} and two different radially averaged values of R/L_T are investigated: $R/L_T \approx 8$ in XGC1p and $R/L_T \approx 11.5$ in GYSELA. The physics of the quantities (a)–(g) may be summarized as follows. For both codes, the heat flux figures 13(a) and 14(a) is the fundamental quantity, which drives all others. Note that bursts in the heat flux appear quasi-regularly in time at the outer boundary in XGC1p and in the central region in GYSELA, as expected from their instability drive. These appear as small, localized 'flamelets' or 'hot spots' in figures 13(a) and 14(a). Intensity pulses, shown in figures 13(b) and 14(b) as linear 'flame tongues', again propagate in time inward in XGC1p and in both directions in GYSELA. They appear to emanate from the heat flux hot spots. In both cases, $\langle(\tilde{T}/T)^2\rangle$ and $\langle\tilde{v}_{||}^2\rangle$ pulses, shown in figures 13(c) and (f) behave similarly. Thus, it is not surprising that structurally similar spatio-temporal pulses appear in the contour plots of residual stress (figure 13(d)) and its associated cross-phase (figure 13(e)). These, too, exhibit the pattern of linear tongues, symptomatic of inward propagation, emanating from the locations of the heat flux 'hot spots' on the outer boundary. This behaviour is consistently found in both codes. In GYSELA since toroidal flow shear is present, a significant diffusive contribution to the Reynolds stress is expected and the residual stress cannot be measured straightforwardly. Assuming a negligible convective term, the residual stress can be estimated [26] by subtracting the diffusive term from the Reynolds stress, assuming the turbulent momentum diffusivity to be $\chi_\phi = \langle\tilde{v}_r^2\rangle\tau_c$ where $\tilde{v}_r$ is the fluctuating radial $E \times B$ velocity and τ_c is the turbulent correlation time. This is shown in figure 14(c). Given this rough estimate for χ_ϕ, an effective Prandtl number $Pr = \chi_\phi/\chi_i$ of order unity is found in GYSELA in the central region where the turbulence is strong, and decreases towards the edge. Finally, $-\tilde{T}$ and $\tilde{v}_{||}$—both of which are advected quantities—appear to be strongly correlated figure 13(g). Note that a striking feature of figures 13(d) and (e) is that they both strongly suggest that residual stress, and thus intrinsic torque, build *inward* from the boundary region in regimes where the turbulence intensity peaks at the edge, as observed in the XGC1p simulation. The mechanism of this build-up is by turbulence intensity pulses (i.e. turbulence spreading [27]) inducing inwardly propagating pulses in the residual stress and intrinsic torque. These inward-propagating momentum transport events then drive the flow

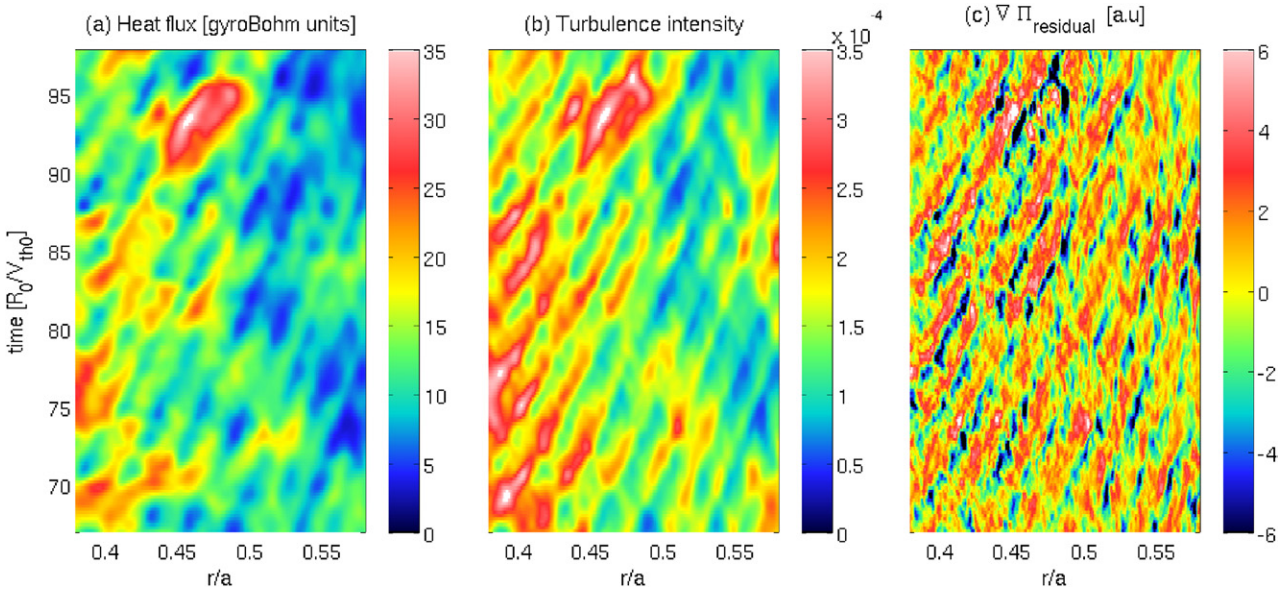

Figure 14. Space–time graphs in GYSELA of (*a*) the normalized heat flux, (*b*) the turbulence intensity and (*c*) the residual stress. The x-axis is normalized minor radius, and the y-axis is normalized time.

profile evolution. One question which is fundamental to this scenario concerns how to understand the relation between (inward) avalanches of *positive* heat flux—corresponding to *outward* propagating heat—and avalanches of *negative* momentum flux, i.e. of residual stress and of intrinsic torque—corresponding to *inward*-propagating parallel momentum. These two phenomena may be reconciled by noting that

(i) generically, intensity profiles increase with radius (apart from ETB plasmas)
(ii) a pulse in heat flux will necessarily produce a surge in the fluctuation level. It is natural, then, for the local fluctuation energy excess to relax by inward spreading. Such inward spreading will naturally appear as inward-propagating intensity fronts which are ignited by bursts in the heat flux. Finally, then, the intensity fronts naturally produce residual stress fronts which drive intrinsic rotation.

In this way, we understand a link between edge heat flux bursts, naturally appearing where ∇T steepens at the beginning of the cooling zone, and the development of intrinsic torque from the outside, inward.

5. Discussions and conclusions

In this paper, we have presented the results of detailed simulation studies of the dynamics of intrinsic torque and rotation profile evolution in flux-driven ITG turbulence. The principal results of this work are:

(i) Significant net unidirectional co-current toroidal rotation, with thermal Mach number $M_{\mathrm{T}} > 0.05$, is observed to develop from noise in flux driven turbulence with an external no-slip boundary condition.
(ii) The intrinsic rotation profile in XGC1p builds inwards, from the boundary, as observed in some experiments [28] and more generally, as shown through the GYSELA results tends to build-up from regions of strong turbulence and then spreads both ways.
(iii) Since the simulation plasma can be held stationary (i.e. local rotation profile flat $\langle v_{||} \rangle \approx 0$ with direct counter-current momentum, the existence of a local intrinsic torque is demonstrated. The intrinsic torque is responsible for the self-acceleration of the plasma from rest. The intrinsic torque is observed to scale linearly with R/L_T.
(iv) The intrinsic torque density is due to the divergence of a residual stress (i.e. $\tau_{\mathrm{intr}} = -\partial_r \Pi_{\mathrm{resid}}$), as the diffusive component of the toroidal Reynolds stress is negligible during the time of the simulation.
(v) The measured intrinsic torque is correlated with both the mean $E \times B$ shear $\langle V_E \rangle'$ and the mean turbulence intensity gradient I', both of which are candidate symmetry breaking mechanisms which can set the sense of the residual stress. Interestingly, the measures of correlation of Π_{resid} with $\langle V_E \rangle'$ and I' are approximately equal, suggesting that mechanisms other than the conventional $E \times B$ shear may determine the residual stress.
(vi) The normalized probability distribution function of the heat flux (positive, leading to outward propagation of heat) and of the momentum flux while the intrinsic rotation builds (negative in XGC1p leading to inward propagation of momentum and both positive and negative in GYSELA due to a different excitation of the turbulence) show interesting trends: both PDFs are very similar in XGC1p and nearly overlay one another in the regions where a strong Reynolds stress is observed whilst they differ in GYSELA. Interestingly in that case the heat PDF remains strongly skewed whilst the momentum PDF is more symmetric. This is likely due to the central excitation of the turbulence which allows for a symmetry between incoming and outgoing avalanches. In other words, heat and momentum are found to be transported by the same avalanches, but heat propagates outward (as constrained by the second thermodynamical principle)

while momentum can propagate both ways (note that there is no such thermodynamical constraint on the propagation direction of momentum). The observation with both codes of inward-propagating avalanches is further evidence that a ∇T driven, non-diffusive momentum flux produces the intrinsic rotation profile.

(vii) Increased inward turbulence intensity propagation of fronts triggered by heat avalanches enhances the phase correlation of radial $E \times B$ flow with parallel flow perturbations and so also drives an inward momentum flux. We observe that the intrinsic rotation profile when the turbulence is strong in the edge builds from the outside in.

All told, these results strongly support the model of a turbulence driven intrinsic torque as the origin of intrinsic rotation.

There are aspects of the results which merit more discussion and plans for detailed future study. There are:

(i) the synergy and proximity in XGC1p of the no-slip boundary condition on $\langle v_{||} \rangle$, the edge cooling layer and the *absence* of any fluctuation damping layer near the boundary are *all* required to realize significant self-acceleration. In particular, the edge cooling layer, together with strong heat flux drive, produces the requisite steep ∇T near the edge. This steep temperature gradient drives the non-diffusive Reynolds stress (residual stress) which produces the intrinsic torque. That, in turn, acts in concert with the no slip boundary condition to drive the flow. The absence of a fluctuation damping boundary layer, often utilized in global simulations, allows direct transmission of stresses to the wall by turbulence.

(ii) the rather obvious out $\rightarrow$ in dynamics of the flow profile build-up when the turbulence is excited in the edge region. This phenomena, which is similar to the build-up of intrinsic rotation in H-mode [28], appears to result from inward turbulence pulses originating during heat flux bursts near the edge. Since fluctuation intensity is peaked at the edge, the pulse-induced bursts will lead to the inward-propagating pulses of intensity and Reynolds stress. These, in turn, build up the flow. Note the intensity and stress propagate inward, the *sign* of the stress is such as to generate co-rotation. These results merit further study in both gyrokinetic and simpler gyrofluid simulations.

(iii) the existence of a strong correlation between the heat flux and momentum flux PDFs while the rotation profile is building. Specifically, whilst PDF(Q) $\approx$ PDF($-\Pi_{r,\phi}$) in XGC1p it is not so in Gysela, suggesting that during the profile build-up phase, avalanches of heat flux, which is positive due to thermodynamical constraints, may drive avalanches of positive *and* negative momentum flux, leading to both outward *and* inward propagation of momentum. Once $\langle v_\phi(r) \rangle$ builds up, we expect as hinted at in Gysela the PDF(Q) to remain similar, whilst the PDF($-\Pi_{r,\phi}$) should approach symmetry between incoming and outgoing avalanches, driven by $\nabla \langle T_i \rangle$ and $\nabla \langle V_\phi \rangle$, respectively. This will be pursued in future studies with both gyrofluid and gyrokinetic codes.

(iv) the finding that $\tau_{\text{intr}} \sim R/L_T$ supports the 'intrinsic rotation as heat engine' model and suggest further, more in depth studies of this model should be undertaken.

Finally, we should note while that the classic manifestation of intrinsic rotation generation is in H-mode plasmas—to which the famous Rice scaling [1] $\Delta v_\phi \sim \Delta W/I_p$ applies—the phenomena we study here—especially through the choices of the temperature and density profiles in XGC1p—are *not* simulations of H-mode, though there are some similarities. Thus, it is natural to ask, if not H-mode, what physical tokamak operation regime *do* these simulations resemble? We believe the answer is that the simulations resemble a sort of zero torque RI-mode [29–31]. Specifically, the strong edge cooling is similar to a radiative cooling mantle, and tends to steepen ∇T, which then drives the rotation. Of course, were non-adiabatic electrons included, a strong ITG turbulence driven inward particle pinch would steepen ∇n and feedback to reduce the ITG, while possibly triggering TEM and other ∇n-driven instabilities. The physics to represent these phenomena are not in the model. However, our results suggest that steepening of ∇T_i by radiative mantle cooling in RI-mode may drive significant intrinsic rotation, along with density profile steepening and confinement enhancement. Further work on this prediction appears interesting and will be pursued in the future. We hope that possible experiments will be considered, as well. We note that studies of intrinsic rotation in RI-mode, p-ITB [32] and IOC [33] regimes have not been performed and would be of significant potential interest.

Acknowledgments

The authors thank Ö.D. Gürcan, C. McDevitt, J. Rice and G. Tynan for stimulating discussions. This work was supported by the World Class Institute (WCI) Program of the National Research Foundation of Korea (NRF) funded by the Ministry of Education, Science and Technology of Korea (MEST) (NRF Grant Number: WCI 2009-001) and National R&D Program (2011-0018728), by the US DOE Contract No DE-FC02-08ER54959 and DE-FG02-06ER54845. The work with XGC1p used resources of the Oak Ridge Leadership Computing Facility, which is supported by the Office of Science of the Department of Energy under Contract DE-AC05-00OR22725, and resources of the National Energy Research Scientific Computing Centre, which is supported by the Office of Science of the US Department of Energy under Contract No. DE-AC02-05CH11231. The work with Gysela was granted access to the HPC resources of CCRT and CINES under the allocation 2009052224 made by GENCI (Grand Equipement National de Calcul Intensif), as well as on HPC-FF in Jülich.

References

[1] Rice J.E. *et al* 2007 *Nucl. Fusion* **47** 1618
[2] Diamond P.H., McDevitt C.J., Gürcan Ö.D., Hahm T.S. and Naulin V. 2008 *Phys. Plasmas* **15** 012303
[3] Diamond P.H., McDevitt C.J., Gürcan Ö.D., Hahm T.S., Wang W.X., Yoon E.S., Holod I., Lin Z., Naulin V. and Singh R. 2009 *Nucl. Fusion* **49** 045002
[4] Solomon W.M. *et al* 2010 *Phys. Plasmas* **17** 056108
[5] Ida K. *et al* 2010 *Nucl. Fusion* **50** 064007
[6] Gürcan Ö.D., Diamond P.H., McDevitt C.J. and Hahm T.S. 2010 *Phys. Plasmas* **17** 032509
[7] Kosuga Y., Diamond P.H. and Gürcan Ö.D. 2010 *Phys. Plasmas* **17** 102313

[8] Idomura Y., Urano H., Aiba N. and Tokuda S. 2009 *Nucl. Fusion* **49** 065029
[9] Ku S., Chang C.S. and Diamond P.H. 2009 *Nucl. Fusion* **49** 115021
[10] Grandgirard V. *et al* 2007 *Plasma Phys. Control. Fusion* **49** B173
[11] Littlejohn R.G. 1985 *Phys. Fluids* **28** 2015
[12] Hahm T.S. 1988 *Phys. Fluids* **31** 2670
[13] Scott B. and Smirnov J. 2010 *Phys. Plasmas* **17** 112302
[14] Abiteboul J., Garbet X., Grandgirard V., Allfrey S.J., Ghendrih Ph., Latu G., Sarazin Y. and Strugarek A. 2011 *Phys. Plasmas* **18** 082503
[15] Parra F.I. and Catto P.J. 2009 *Plasma Phys. Control. Fusion* **51** 095008
[16] Parra F.I. and Catto P.J. 2010 *Phys. Plasmas* **17** 056106
[17] Lee W.W. 1983 *Phys. Fluids* **26** 556
[18] Wang L. and Hahm T.S. 2010 *Phys. Plasmas* **17** 082304
[19] Sarazin Y. *et al* 2011 *Nucl. Fusion* **51** 103023
[20] Dif-Pradalier G. *et al* 2011 *Phys. Plasmas* **18** 062309
[21] Rice J.E. *et al* 2011 *Phys. Rev. Lett.* **106** 215001
[22] Coda S. 2011 *Nucl. Fusion* **51** 094017
[23] Gürcan Ö.D., Diamond P.H., Hahm T.S. and Singh R. 2007 *Phys. Plsmas* **14** 042306
[24] Gürcan Ö.D., Diamond P.H., Hennequin P., McDevitt C.J., Garbet X. and Bourdelle C. 2010 *Phys. Plasmas* **17** 112309
[25] Wang W.X., Hahm T.S., Ethier S., Rewoldt G., Lee W.W., Tang W.M., Kaye S.M. and Diamond P.H. 2009 *Phys. Rev. Lett* **102** 035005
[26] Yan Z., Xu M., Diamond P.H., Holland C., Müller S.H., Tynan G.R. and Yu J.H. 2010 *Phys. Rev. Lett.* **104** 065002
[27] Gürcan Ö.D., Diamond P.H. and Hahm T.S. 2007 *Phys. Plasmas* **14** 055902
[28] Rice J.E. *et al* 2004 *Nucl. Fusion* **44** 379
[29] Ongena J. *et al* 1993 *Proc. 20th European. Conf. (Lisbon, Portugal)* vol 17C p 127
[30] Messiaen A. *et al* 1996 *Phys. Rev. Lett.* **77** 2487
[31] Messiaen A. *et al* 1997 *Phys. Plasmas* **4** 1690
[32] Xiao W.W. *et al* 2010 *Phys. Rev. Lett.* **104** 215001
[33] Soldner F.X. *et al* 1988 *Phys. Rev. Lett.* **61** 1105